

Neutronic and mechanical evaluation of rare earth doped and undoped nitride-based coatings for accident tolerant fuels

E. Alat ^{a,*}, M.J. Brova ^a, I.M. Younker ^b, A.T. Motta ^{a,b}, M. Fratoni ^c, D.E. Wolfe ^{a,d}

^a Department of Materials Science and Engineering, The Pennsylvania State University, University Park, PA, 16802, USA

^b Department of Mechanical and Nuclear Engineering, The Pennsylvania State University, University Park, PA, 16802, USA

^c Department of Nuclear Engineering, University of California, Berkeley, CA, 94720-1730, USA

^d Applied Research Laboratory, The Pennsylvania State University, 119 Materials Research Building, University Park, PA, 16802, USA

ARTICLE INFO

Article history:

Received 9 July 2018

Received in revised form

24 February 2019

Accepted 25 February 2019

Available online 2 March 2019

Keywords:

Accident tolerant fuel

Cathodic arc physical vapor deposition

Titanium nitride

Titanium aluminum nitride

Rare earth doping

Neutronic analysis

ABSTRACT

As a part of the effort to develop accident-tolerant fuel (ATF) that would delay potential deleterious consequences of loss-of-coolant-accidents (LOCA), TiN and TiAlN coating application on nuclear fuel claddings were shown as a promising path to enhance corrosion resistance of nuclear fuel cladding. Recently, ytterbium doping was shown to contribute to improving TiAlN coating corrosion performance. However, overall cladding coating performance evaluation requires investigation of neutronic penalties and mechanical properties in addition to corrosion resistance. The current study is composed of two parts. First, the neutronic impact of adding monolithic TiN, monolithic TiAlN and 8-layer TiAlN/TiN coatings (with and without Yb dopants) to the exterior of conventional zirconium-alloy cladding was investigated. Second, an experimental investigation was performed through the deposition of select coating design architecture using cathodic arc physical vapor deposition process onto ZIRLO[®] 1 sheets followed by mechanical testing to examine the adhesion and hardness of the coatings. Characterizations were performed using optical microscopy (OM), scanning electron microscopy (SEM), energy dispersive spectroscopy (EDS), electron probe microanalysis (EPMA), Raman spectroscopy and X-ray diffraction (XRD). It is concluded that to minimize the neutronic penalties, a limitation on the concentration of Yb-dopant is necessary. Mechanical testing showed that hardness decreased with increasing Yb content. The adhesion of the TiAlN coatings was not affected by doping but was affected by the cathode composition.

Published by Elsevier B.V.

1. Introduction

Nuclear energy is one possible contribution to solving the world's energy problems since it is a highly efficient, low cost, and clean energy source [1]. A light water reactor (LWR) nuclear fuel assembly is composed of about 200 tubes kept in place by spacer grids. These tubes include both guide tubes and fuel rods containing enriched uranium dioxide (or a mixture of uranium and plutonium oxide in the case of MOX fuel) ceramic fuel pellets stacked in the cladding tube [2]. The cladding separates the fuel pellets from the surrounding coolant water, thus functioning as a

barrier to avoid fission products release while being almost transparent to neutrons and allowing heat transfer to the coolant water [2,3]. Zirconium-based alloys have been widely used as LWR cladding materials because of their low neutron absorption cross-section, adequate mechanical properties and good corrosion resistance in water near 300 °C [4–6]. Cladding performance is highly challenged in accident conditions with possible generation of hydrogen that can lead to hydrogen explosions. A recent example occurred in the Fukushima-Daiichi accident, in which a station blackout caused a loss-of-coolant and progressed to a beyond-design-basis accident. This has motivated research into Accident Tolerant Fuels (ATFs), which are defined as fuels that provide additional coping time in the case of a loss of active cooling in the reactor core, making external intervention possible before severe fuel damage occurs [7,8]. These fuels are designed to improve the performance, reliability, and safety of conventional UO₂/zirconium-alloy fuel during beyond design basis accident conditions and

* Corresponding author.

E-mail addresses: alatece@yahoo.com (E. Alat), mjb5893@psu.edu (M.J. Brova).

¹ ZIRLO[®] is a registered trademark of the Westinghouse Electric Company LLC, its Affiliates and/or Subsidiaries in the United States of America and may be registered in other countries throughout the world. All rights reserved. Unauthorized use is strictly prohibited. Other names may be trademarks of their respective owners.

improve performance, both during normal operations and during design-basis accidents. Specifically, ATF should prevent or at least significantly slow down hydrogen formation from the interaction of zirconium with high temperature steam.

There are several ATF approaches in literature. Candidate technologies include coated Zr-based alloys [8–13], SiC/SiC [8,14–28], SiC ceramic matrix composite/Zr-based alloy hybrids [8], advanced Zr-based alloys [8], Zr-based alloy or FeCrAl coated Mo-alloys [7,29,30], FeCrAl [31], Ti₃SiC₂ [30], Ti₂AlC [30] and engineered stainless steel alloys [7,8,30,32,33]. These ATF cladding concepts can be grouped into three categories: (i) full cladding replacement, (ii) hybrid and (iii) protective coating applications. To prove viable, ATF concepts should be easy to implement within the framework of current and future LWRs, and to exceed or at least match current LWR fuel performance. Among various ATF concepts, a protective coating application is one of the most promising approaches since it could improve the corrosion characteristics of the currently used Zr-based alloy claddings without requiring a major change in cladding design. Many coating approaches for Zr-based alloy substrates have been previously proposed including metallic, nonmetallic, oxide, carbide, nitride and multilayer coating designs [4,8–13,34,35]. The challenges regarding a protective coating application include the requirement for low neutronic penalty, ease of fabrication, scalability of the deposition method for production-size components, adhesion of the coating to the substrate, and thermal and mechanical compatibility of the coating and the substrate material both at normal and accidental environment conditions [35].

Transition metal nitrides provide enhanced hardness, wear resistance and chemical inertness due to a mixed bonding structure involving ionic, covalent and metallic bonds [36]. TiN and TiAlN coatings have been widely used for years on high-speed tool steels, cemented carbides, and cermet substrates for various cutting and finishing operations in the tooling industry [36–43]. Several physical vapor deposition (PVD) methods can be used to deposit these coatings such as magnetron sputtering, anodic arc ion plating, electron arc ion plating and cathodic arc ion plating [44]. Among these, cathodic arc physical vapor deposition (CA-PVD) is a line-of-sight deposition process which has several advantages over other PVD processes, such as energetic particle bombardment on the substrate surface leading to good adhesion, dense coating formation, coating microstructure improvement, grain size reduction, microhardness enhancement due to high preferred orientation, and the development of compressive stresses that help terminate crack propagation, tailorability of the interfacial products (especially in multilayer coatings), and scalability to production size components [36,45–48]. Previously, the corrosion behavior of single-layer TiN, single-layer TiAlN and multilayer TiN/TiAlN coating design architectures deposited on ZIRLO[®] substrates using CA-PVD and tested in static pure water at 360 °C and 18.7 MPa was investigated, although higher temperature investigation is still necessary, current results are found to be promising [49,50]. To extend the good behavior to higher temperatures, doping with chromium and yttrium are possible [51]. Recently, ytterbium doping contribution to advance corrosion resistance of single-layer TiAlN coating deposited on ZIRLO[®] substrates using a hybrid coating technique of resistance evaporation and CA-PVD was also demonstrated [52]. However, the viability of these coating designs for nuclear fuel cladding applications depends on an investigation of mechanical properties and the neutronic penalty.

Neutronically, each TiAlN coating, whether the 8-layer TiAlN/TiN or the doped 8-layer TiAlN/TiN, introduces parasitic neutron absorption into every fuel assembly. It is necessary to calculate the percentage of neutrons absorbed within each coating layer, quantify the effect of the added neutron absorption on fuel cycle length,

and present design solutions to maximize fuel performance without sacrificing accident tolerance. For lattice-level neutronic investigations, the SERPENT Monte Carlo code and SCALE 6.1 package TRITON, KENO-VI, CENTRM modules have been previously used in literature [53–58]. Previously, a neutronic penalty investigation was performed for Ti_{0.5}Al_{0.5}N using the SERPENT Monte Carlo Code, which concluded that a 10–30 μm coating thickness would result in minimal neutronic penalty [58].

There are considerations in developing coatings, which are initially mentioned in this section, but the current study will discuss neutronic penalty and mechanical property effects of doped and undoped single-layer TiAlN, single-layer TiN and multilayer TiN/TiAlN coatings on Zr-based alloy nuclear fuel claddings. The study was conducted in two parts. First, the neutronic impact of adding monolithic TiN, monolithic TiAlN and 8-layer TiAlN/TiN coatings with and without dopants to the exterior of conventional UO₂/zirconium-alloy cladding was investigated. Second, an experimental investigation was performed through deposition of select coating designs using CA-PVD method on ZIRLO[®] sheets and mechanical testing to examine adhesion and hardness of the coatings. High temperature performance investigation will be considered as a future study.

2. Neutronic model and methodology

The SERPENT Monte Carlo code [59] is used to evaluate the neutronic performance of single-layer doped and undoped TiAlN, and 8-layer TiN/TiAlN coatings. The selected reference pressurized water reactor (PWR) was the Westinghouse AP1000 with a 17 × 17 fuel assembly [60]. Such an assembly contains 264 fuel rods, 24 guide thimbles, and 1 instrumentation thimble. Reflective boundary conditions on four sides generate an infinite radial lattice with finite axial length. The assembly extremities contain axial reflectors composed of a water and steel mixture (50%–50% volume mix, 100 cm length). Core parameters are shown in Table 1 [60]. Cycle length and attainable burnup were projected from the depletion of a single assembly averaged reactivity under the assumption of constant power throughout the lifetime of the assembly [61]. To correct for the infinite lattice model, radial leakage was assumed to be 3% [61]. Neutronic analysis for single-layer TiAlN, single-layer TiN and 8-layer TiAlN/TiN used ENDF/B-VII.0 cross sections. However, since ENDF/B-VII.0 does not contain Yb cross section data, the JEFF 3.1.1 cross section data was used for all doping calculations. Cross sections were Doppler broadened at the following temperatures: 784 °C for fuel, 364 °C for clad, 327 °C for coolant, and thermal scattering cross sections were applied to the water. Depletion calculations used Chebyshev Rational Approximation Method (CRAM) and a high-resolution flux spectrum based on the unified energy-grid structure to calculate one-group cross sections.

The reference UO₂ was assumed to be 4.5 at.% enriched and Zircaloy-4 (0.1 wt% Cr, 0.21 wt% Fe, 1.45 wt% Sn, and 98.24 wt% Zr;

Table 1
The reference pressurized water reactor (PWR) design core parameters [60].

Property	Value
Total power, MW	3400
Assemblies	157
Core average coolant temperature, °C	303
Pressure, bar	155
Core average coolant density, °C	0.719
Active length, cm	426.72
Pellet diameter, cm	0.82
Clad thickness, cm	0.057
Fuel rod outer diameter, cm	0.95
Pitch-to-diameter ratio	1.326

6.56 g/cm³) was chosen as the reference cladding material. The reference cycle length was found to be 446.5 EFPD (effective full power days) with ENDF/B-VII cross section data or 445.5 EFPD with JEFF 3.1.1 cross section data. The fuel enrichment compensation was determined as described in Younker et al. [58].

3. Experimental methods

3.1. Materials and coating

ZIRLO[®], a Zr-based alloy having a composition of 1 wt% Nb, 1 wt% Sn, 0.1 wt% Fe and balance Zr, was used as the substrate material. In the present study, ZIRLO[®] was provided in sheet form by Westinghouse Electric Company LLC (Pittsburgh, PA). The thickness of the ZIRLO[®] sheets was 0.05 cm. These sheets were cut to dimensions of 5 cm × 2.5 cm × 0.05 cm using a diamond saw. Prior to coating deposition, the substrate surface was prepared by hand grinding with either 320-grit SiC paper or Green Scotch-Brite scouring pads (240 grit Al₂O₃) to remove oxides and obtain a substrate surface roughness value of 0.25 μm R_a, which was previously determined to be the optimum value for good adhesion between the ZIRLO[®] substrate and the coating [49]. Then, substrates were cleaned using ultra-sound in acetone and methanol for 10 min per each, rinsed with deionized water and dried with pure nitrogen gas (99.999%).

3.2. Coating deposition

CA-PVD was used to deposit single-layer TiAlN, single-layer TiN and 8-layer TiN/TiAlN coatings onto the ZIRLO[®] sheets. The CA-PVD chamber was a cubic chamber with 50.8 cm side. Cylindrical solid cathodes had 6.3 cm diameter and 3.2 cm thickness. The ZIRLO[®] substrates were mounted in a planet-sun rotation arrangement where the substrates represent the planets and individually rotate clockwise at 6.75 rpm as well as the entire sample holder which also rotates clockwise at 2.4 rpm. The chamber temperature was set to 325 °C. First, ion etching was performed by applying 1.6 × 10⁻³ Pa Ar atmosphere and -1000 V substrate bias to remove the native oxides from the substrate surface. Then, a 0.6 μm thick titanium bond coating (Ti-BC) layer was deposited onto ZIRLO[®] using a pure titanium cathode (99.999%), 65 A arc current and -150 V substrate bias in 1.6 Pa Ar atmosphere, as was done in Ref. [49]. Undoped TiAlN layer deposition was performed using cathodes with a composition of either Ti_{0.33}Al_{0.67} or Ti_{0.20}Al_{0.80} in 1.6 Pa N₂ atmosphere using 45–65 A arc current and 0(-100) V substrate bias. TiN layer deposition was performed with the same parameters used during the Ti-BC layer deposition except that the TiN deposition took place in 1.6 Pa N₂ atmosphere instead of Ar atmosphere.

For Yb-doped TiAlN coating deposition, the CA-PVD system was modified to achieve a hybrid coating technique combining resistance evaporation and CA-PVD. Details of the ytterbium doping during the TiAlN coating deposition and the schematic image of the modified deposition chamber were provided in Brova et al. [52]. Resistive thermal evaporation of ytterbium was used in situ to dope the outer half of the Ti_xAl_{1-x}N coatings during CA-PVD deposition. The power supply ran high voltage through a high current transformer which led the current through a specially designed thermal evaporation unit. Ytterbium metal was placed on tantalum evaporation boats of different sizes where the current would resistively heat the dopant species. The different tantalum boat sizes changed the resistance which in turn would change the amount of current used to evaporate the ytterbium which allowed for the generation of different dopant concentrations. A nitrogen gas flow line at 17 sccm was used to direct the ytterbium vapor species to the samples

during the deposition process. The sample deposition parameters are summarized in Table 2.

3.3. Testing and characterizations

Scratch testing was performed to determine the adhesion strength of the coatings according to ASTM C1624: Standard test method for adhesion strength and mechanical failure modes of ceramic coatings by quantitative single point scratch testing [62]. The test was performed using a Romulus IV Universal Materials Tester (Spokane, WA, USA). Microhardness indentation testing was performed using a Leco MHT Series 200 indenter (St. Joseph, MI, USA) with a Vickers tip at a load of 10 g.

Characterizations were performed using optical microscopy (OM), scanning electron microscopy (SEM), energy dispersive spectroscopy (EDS), electron probe microanalysis (EPMA), optical profilometry, Raman spectroscopy and X-ray diffraction (XRD). OM and SEM were utilized for high resolution imaging. On FEI Quanta 200 Environmental SEM instrument was used for SEM analysis which was performed both in secondary electron mode (SEM-SE) and in backscattered electron mode (SEM-BSE). Examinations were performed both on surface and cross-section samples. Cross-sectional samples were coated with iridium to avoid charging during electron microscopy measurement. The coating thicknesses were measured using ImageJ from cross-section SEM-BSE images. The average coating thicknesses were determined by 15 data collected from SEM-BSE images taken from five different locations on both sides of the coating. EDS and EPMA were performed to identify and quantify the chemical composition of the samples in the as-deposited coating. The EDS analysis was conducted by utilizing EDS equipment mounted to the scanning electron microscopy instrument. Chemical composition measurement was performed on cross-section samples with the help of AzTEC software used in the point analysis mode. To identify the energy peaks obtained during EDS analysis, standard values embedded to the AzTEC software were used. The coating chemical compositions were measured from five different locations on both sides of the coating (3-measurement locations from one side, 2-measurement locations from the other side). The chemical composition measurement was performed from the middle of the coating thickness. Optical profilometry was used to determine substrate surface roughness. Raman spectroscopy and XRD scans were performed to determine coating phases. XRD patterns were obtained with the PANalytical XPert Pro Multi-Purpose Diffractometer (MPD). The 2θ scan was performed using Cu K_α radiation (K_{α1} = 1.54056 Å, K_{α2} = 1.54443 Å) with fixed divergence slit (0.25°), receiving slit (0.25°), and a step size of 0.026°. XRD analysis was performed on the surface of the flat and tubular samples. Two different XRD scans were acquired, which included normal Bragg-Brentano (XRD-BB) and Grazing Incidence (GIXRD). XRD pattern identifications were performed using JADE software.

4. Results

This study has been conducted with the aim of investigating the neutronic penalty and the mechanical properties of nitride coatings recently developed to enhance the performance of nuclear fuel claddings as an accident tolerant fuel. The investigated coating designs involved doped and undoped single-layer TiAlN, single-layer TiN, 8-layer TiN/TiAlN.

4.1. Neutronic analysis

To understand the neutronic impact of each coating layer, the 8-layer TiAlN/TiN multilayer coating was broken into its basic

Table 2
Nitride-based coating cathodic arc physical vapor deposition process parameters. Deposition parameters are presented for (TiAlN/TiAlN + Yb)/TiN in the specified order.

Coating	TiAl cathode composition, Ti/Al (at.%)	Deposition time (min)	Substrate bias (V)	Source current (A)	Current through Yb (A)	Yb plasma evaporation (min)
TiAlN	20/80	(450/0)/0	(0/0)/0	(60/0)/0	0	0
TiAlN	20/80	(450/0)/0	(25/0)/0	(60/0)/0	0	0
TiAlN	20/80	(450/0)/0	(50/0)/0	(60/0)/0	0	0
TiAlN	20/80	(450/0)/0	(100/0)/0	(60/0)/0	0	0
TiAlN	33/67	(450/0)/0	(50/0)/0	(60/0)/0	0	0
8-layer TiN/TiAlN	20/80	4x[(50/0)/50]	4x[(75/0)/150]	4x[(45/0)/45]	0	0
8-layer TiN/TiAlN	33/67	4x[(50/0)/50]	4x[(75/0)/150]	4x[(45/0)/45]	0	0
TiAlN + Yb (0.44 at.%)	33/67	(120/120)/0	(50/50)/0	(45/45)/0	170	30
TiAlN + Yb (0.64 at.%)	33/67	(60/180)/0	(50/50)/0	(45/45)/0	116	180
TiAlN + Yb (4.78 at.%)	33/67	(120/120)/0	(50/50)/0	(45/45)/0	165	66
TiAlN + Yb (19.72 at.%)	33/67	(120/120)/0	(50/50)/0	(45/45)/0	180	120
TiAlN + Yb (33.24 at.%)	33/67	(120/120)/0	(50/50)/0	(45/45)/0	200	120

components, pure TiN, $Ti_{0.20}Al_{0.80}N$, and $Ti_{0.33}Al_{0.67}N$. Each coating was applied at thicknesses of 4, 8, and 12 μm and included the 0.6 μm Ti-BC layer. Table 3 shows the percentage of neutron loss due to absorption within coating and the corresponding cycle length penalty as compared to the uncoated case. Two major trends can be observed: (1) the percentage of neutrons absorbed within the coating increases linearly with coating thickness; (2) the overall absorption is driven by the most absorbing element, titanium. Accordingly, TiN absorbs more neutrons than either $Ti_{0.20}Al_{0.80}N$ or $Ti_{0.33}Al_{0.67}N$. The Ti-BC layer composition and thickness remained constant resulting in an unvarying percentage of absorbed neutrons in the bond coating, 0.01%. Parasitic absorption associated with each coating leads to fewer neutrons available for fission, decreases reactivity, and ultimately shortens fuel cycles. The resulting EFPDs follow the trends of neutron absorption percentage. However, the neutronic penalties stemming from $Ti_{0.20}Al_{0.80}N$, and $Ti_{0.33}Al_{0.67}N$ coatings are minor and can be compensated by a slight increase to fuel enrichment (<0.05 at.%).

The neutronic penalty of 8-layer TiN/TiAlN having a coating thickness of 8 and 12 μm was also investigated. To determine the neutronic penalty in the case of 8-layer TiN/TiAlN coatings, layers of TiN, $Ti_{0.20}Al_{0.80}N$, and $Ti_{0.33}Al_{0.67}N$, 1 and 1.5 μm thick, combined in an alternating pattern along with a 0.6 μm Ti-BC layer were assumed. Table 4 shows the percentage of neutrons captured and cycle length penalty caused by the entire coating (including 0.01% from Ti bond layer) and individual components. As expected, neutron absorption and cycle length penalty follow the trends previously described for single-layer TiN and single-layer TiAlN coating. One would envision total coating absorption and cycle length penalty values for 8-layer TiN/TiAlN to lie between those of pure TiN and TiAlN, which they do. As in the case of single-layer coatings, neutronic penalties are low and an increase in enrichment of less than 0.08 at.% could be enough to maintain the reference cycle length.

Finally, the neutronic penalty effect of Y and Yb doping on TiAlN coating was investigated through consideration of four dopant

Table 3
Percentage of neutrons absorbed within the coating/Cycle length penalty (EFPD) derived from coatings as a function of the monolithic coating composition and thickness.

Coating	Thickness, μm		
	4	8	12
TiN	0.12/-2.8	0.24/-5.1	0.37/-8.0
$Ti_{0.20}Al_{0.80}N$	0.05/-1.1	0.10/-2.5	0.15/-4.0
$Ti_{0.33}Al_{0.67}N$	0.06/-1.5	0.11/-2.7	0.17/-4.3

concentrations: 1, 2, 5, and 10 wt%. TiAlN layers were doped with either Y, Yb, or a 50%–50% mixture of both. Investigated doping concentrations and corresponding cycle length penalty values are summarized in Table 5. To provide the most conservative analysis, the 8-layer TiAlN/TiN with the highest neutronic penalty was doped, in this case 12 μm thick $Ti_{0.33}Al_{0.67}N$ /TiN. TiN layer composition remained constant. $Ti_{0.33}Al_{0.67}N$ compositions incorporated the dopant concentrations, while scaling the previous $Ti_{0.33}Al_{0.67}N$ composition accordingly. $Ti_{0.33}Al_{0.67}N$ densities were also adjusted to account for denser doping agents. Microscopic radiative capture cross sections at 327 °C for titanium, yttrium, and ytterbium, and percentage of neutrons captured within doped 12 μm 8-layer TiN/ $Ti_{0.33}Al_{0.67}N$ coating as a function of dopant and concentration are presented in Fig. 1. The neutron absorption cross-section of yttrium is lower than that of titanium. Thus, the cycle length penalty (Table 5) and coating absorption (Fig. 1a) scale inversely with yttrium concentration. Conversely, ytterbium possesses an absorption cross section much larger than that of titanium, leading to an increased neutronic penalty. A linear progression of neutron capture for the entire 12 μm 8-layer $Ti_{0.33}Al_{0.67}N$ /TiN coating was observed when doped with Y, Yb, and a Y/Yb mixture (Fig. 1b). As one would expect, the Y/Yb mixture produces results in between those of Y and Yb. Dopant limits are not needed when using yttrium, but strong consideration should be given to minimizing the ytterbium dopant concentration. However, the worst-case scenario (10 wt% Yb) requires less than 0.1 at.% fuel enrichment increase to maintain the reference cycle length.

4.2. As-deposited coating analysis

The coatings were deposited using cathodic arc physical vapor deposition. The method provides flexibility in terms of coating properties by varying deposition parameters such as cathode composition, nitrogen partial pressure, substrate bias and arc current. The starting point for the deposition parameters used in this study were based on our previous studies [49,50,52]. The arc current was determined not to have a significant effect on the deposited coating properties [38]. Thus, in this study we used two different arc current values of 60 A and 45 A to deposit single-layer TiAlN, and 8-layer TiN/TiAlN and Yb-doped TiAlN, respectively. Starting from that point, we further investigated substrate bias and cathode composition effects on coating adhesion. These results are presented here.

In our previous study [49], an increase in the negative substrate bias from 50 to 100 V only slightly enhanced the corrosion performance of the TiAlN coatings. In this study, we further investigated the substrate bias effect by considering four different substrate

Table 4

Percentage of neutrons absorbed within each coating component/Cycle length penalty (EFPD) derived from multilayer coatings as a function of the 8-layer coating composition and thickness.

Alternating layers	Layer thickness, μm	Total coating thickness, μm	Neutron absorption, %			Cycle length penalty, EFPD
			TiAlN	TiN	Total	
Ti _{0.20} Al _{0.80} N/TiN	1	8	0.05	0.12	0.18	-4.1
Ti _{0.33} Al _{0.67} N/TiN			0.06	0.12	0.19	-4.2
Ti _{0.20} Al _{0.80} N/TiN	1.5	12	0.07	0.18	0.27	-5.7
Ti _{0.33} Al _{0.67} N/TiN			0.08	0.18	0.28	-6.0

Table 5

Cycle length penalty (EFPD) derived from doped 12 μm 8-layer TiN/Ti_{0.33}Al_{0.67}N coating as a function of dopant and concentration. Coating absorption and cycle length penalty trend inversely with yttrium concentration.

Dopant	Density, g/cm ³	Composition, wt.%					Composition, at.%					Cycle length penalty, EFPD
		N	Al	Ti	Y	Yb	N	Al	Ti	Y	Yb	
None	3.56	29.2	37.5	33.3	0	0	50.00	33.32	16.68	0	0	0
Y1	3.56	28.9	37.1	33	1	0	49.86	33.22	16.65	0.27	0.00	-6.2
Y2	3.57	28.6	36.8	32.6	2	0	49.70	33.18	16.57	0.55	0.00	-6.2
Y5	3.61	27.8	35.6	31.6	5	0	49.38	32.81	16.41	1.40	0.00	-5.9
Y10	3.67	26.2	33.8	30	10	0	48.44	32.43	16.22	2.91	0.00	-5.4
Yb1	3.6	28.9	37.1	33	0	1	49.93	33.26	16.67	0.00	0.14	-6.5
Yb2	3.64	28.6	36.8	32.6	0	2	49.83	33.27	16.61	0.00	0.28	-6.6
Yb5	3.78	27.8	35.6	31.6	0	5	49.72	33.04	16.53	0.00	0.72	-6.9
Yb10	4	26.2	33.8	30	0	10	49.14	32.89	16.45	0.00	1.52	-7.6
Y0.5/Yb0.5	3.58	28.9	37.1	33	0.5	0.5	49.90	33.24	16.66	0.14	0.07	-6.5
Y1/Yb1	3.61	28.6	36.8	32.6	1	1	49.77	33.23	16.59	0.27	0.14	-6.4
Y2.5/Yb2.5	3.7	27.8	35.6	31.6	2.5	2.5	49.55	32.92	16.47	0.70	0.36	-6.6
Y5/Yb5	3.84	26.2	33.8	30	5	5	48.79	32.66	16.34	1.47	0.75	-6.9

biases of 0 V, 25 V, 50 V and 100 V. The arc current was set as 60 A and Ti_{0.20}Al_{0.80} cathode was used to deposit coatings. GIXRD was used to identify the crystal structure of the phases in the coating (Fig. 2). Most of the peak patterns were fitted with the Ti_{0.32}Al_{0.68}N phase diffraction pattern data shown having the ICDD-PDF# 04-017-4686, which is a hexagonal crystal structure. Other peaks were identified as Ti_{0.5}Al_{0.5}N (ICDD PDF# 04-005-5251) and AlN (ICDD PDF# 04-004-4544). Ti_{0.5}Al_{0.5}N has a cubic crystal structure and AlN has a hexagonal crystal structure. X-ray diffraction examination of the coating shows evidence of both the cubic and hexagonal phases. There was (111) peak of the Ti_{0.5}Al_{0.5}N phase, we see that it is slightly shifted to lower angles and broadened as we go higher substrate bias values. One of the reasons for this is the higher titanium content in the coating at higher substrate bias values resulting in expansion of the lattice parameter compared to lower aluminum content state [63,64]. We have higher titanium content at higher bias because titanium ionization is higher compared to aluminum [65,66] and in the case of resputtering from the substrate surface titanium is resputtered less compared to aluminum since titanium is heavier [36]. Another reason is the complex residual stress state in the coating involving high compressive stresses in normal direction to the coating due to higher energy ion bombardment with increased substrate bias leading to lattice expansion parallel to the surface because of the Poisson's effect [67]. This high ion energy bombardment is also the reason of peak broadening at higher substrate biases [64]. Since the data presented in Fig. 2 are grazing incidence patterns, it is not convenient to talk about preferred orientation, but it should be mentioned that {002} texture is observed at lower substrate bias, but {100} texture is observed at higher substrate bias values. Change of texturing with substrate bias was also observed by Ahlgren et al. [48,68]. The occurrence of texture can be attributed to the driving force to lower the overall coating surface energy [68].

Visual examination results, presented in Fig. 3, showed that all coatings had a dark gray color, the substrate bias affected the

coating color tone and the coating texture. 0 V substrate bias led to a matte finish, while other coatings, deposited with 25 V, 50 V and 100 V, showed a glossy finish (Fig. 3a). The surface SEM–SE images (Fig. 3b) demonstrated that the surface of the coating deposited with 0 V substrate bias was full of sphere-like macroparticles in various sizes. This non-smooth surface covered with spherical macroparticles could be the reason of the matte finish observed in the digital image of the coating. This sphere-like macroparticles on the surface indicates low kinetic energy and attractive forces which can cause deviation in the macroparticle geometry. Coatings deposited with 25 V and 50 V substrate bias also had sphere-like macroparticles on the surface. Macroparticles with perturbation in the case of 50 V and a spattered appearance on the surface was observed in the case of 100 V substrate bias. A sphere-like structure indicates solidification of macroparticle before arriving on the surface [69] or a passive deposition without high enough momentum distort the shape of the macroparticle. Perturbation of macroparticles observed in the case 50 V can be attributed to arrival on the substrate surface in liquid state [69] or distortion in its geometry due to substrate bias. The spatter appearance of the 100 V substrate bias deposited coatings can be attributed to the high momentum of the macroparticles resulting from the high substrate bias [36]. Substrate bias effect on the amount of macroparticles were previously demonstrated in literature [70–73]. Paldey et al. [73] attributed the increase in macroparticle amount to the increase in aluminum content in the coating. Kale et al. [72] attributed the high value of macroparticles at medium bias to the positive charging of macroparticles due to collisions with ions with increased velocity; whereas, macroparticle amount decrease at high bias voltage was attributed to evaporation of them before reaching to the substrate because of excess ion energy. In this study, Al/Ti atomic ratio was ~4 matching the cathode composition and no significant aluminum content variation with substrate bias was observed during the EDS analysis (8.5 ± 0.4 at.% Ti, 32.7 ± 0.4 at.% Al and 56.9 ± 2.1 at.% N). Thus, the lower macroparticle amount with

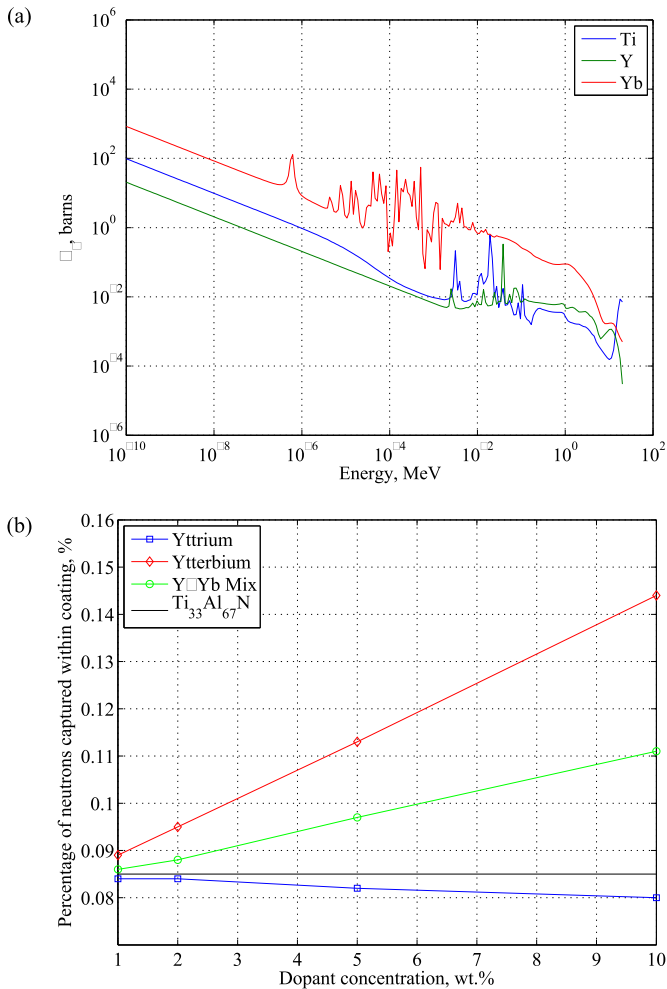


Fig. 1. (a) JEFF 3.1 microscopic radiative capture cross sections at 327 °C (600 K) for titanium, yttrium, and ytterbium. (b) Percentage of neutrons captured within doped 12 μm 8-layer TiN/Ti_{0.33}Al_{0.67}N coating as a function of dopant and concentration.

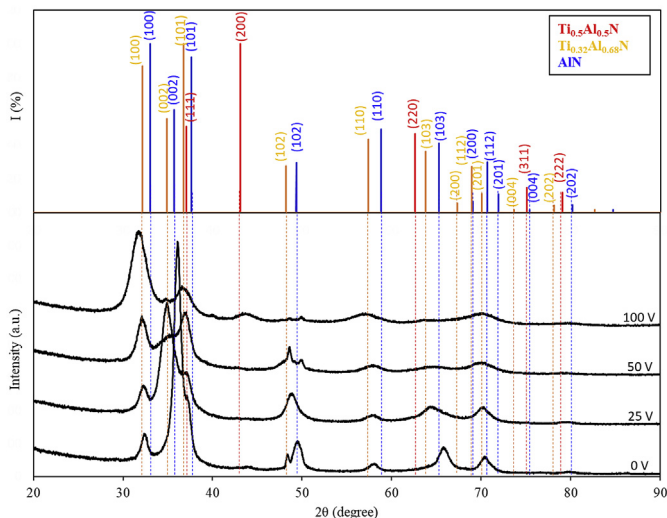


Fig. 2. GIXRD measurement patterns of coatings deposited with 0V, 25V, 50V and 100V. GIXRD was performed using a Cu-K α (1.54048 Å) radiation and with a grazing incidence angle of 1°.

increased substrate bias could be the negative charging of the macroparticles in the plasma and repelling at the substrate surface [70] or evaporation due to high ion energy collision [72]. The cross-section SEM-BSE images presented in Fig. 3c showed that the average TiAlN coating thicknesses of coatings deposited with 0 V, 25 V, 50 V and 100 V were $14.7 \pm 0.5 \mu\text{m}$, $11.2 \pm 0.6 \mu\text{m}$, $13.1 \pm 1.5 \mu\text{m}$ and $3.9 \pm 1.2 \mu\text{m}$, respectively. The lowest coating thickness observed in the case of 100 V substrate bias was attributed a high degree of resputtering from the substrate surface. So, there is an optimum substrate bias value that provides a smooth surface with minimum macroparticles, dense structure with minimum porosity and good adhesion with no delamination. Thus, a 50 V substrate bias satisfied these qualities as compared to the other substrate bias values examined for the deposition conditions studied.

Next, single-layer TiAlN coatings deposited with two different cathode compositions were investigated. The overlaid Raman spectroscopy spectrums (Fig. 4) demonstrated that TiAlN coating deposited with 33 at.% Ti – 67 at.% Al cathode showed two broad bands having peaks at 257 and 673 cm^{-1} ; whereas, TiAlN coating deposited with 20 at.% Ti – 80 at.% Al. TiAlN showed four peaks at 190, 485, 625 and 774 cm^{-1} . Both spectrums demonstrated peaks relevant to TiAlN phase [74,75]. Total spectral density, i.e., the gap between the acoustic and optic modes, between the two broad bands increased in the case of 20 at.% Ti – 80 at.% Al cathode deposited TiAlN coating compared to the 33 at.% Ti – 67 at.% Al cathode deposited TiAlN coating, which is because of more aluminum atoms occupying titanium sites causing more deviation from perfect face centered cubic crystal structure [74,75]. Fig. 5 shows the overlaid GIXRD measurement patterns of coatings deposited with cathodes having a composition of either 33 at.% Ti – 67 at.% Al or 20 at.% Ti – 80 at.% Al. For a cathode composition of 67 at.% Al, coating phase is determined to be Ti_{0.5}Al_{0.5}N (ICDD PDF# 04-005-5251), which has a cubic crystal structure. For a cathode composition of 80 at.% Al, peak patterns were fitting with the Ti_{0.32}Al_{0.68}N phase (ICDD-PDF# 04-017-4686) and AlN (ICDD PDF# 04-004-4544), which have hexagonal crystal structure. It should be noted that slight peak shifting was observed due to slight deviation in the coating chemistries from the ICDD card number. Peaks appeared in a broad manner indicating nanocomposite crystal structure.

Additionally, TiAlN coating chemical composition was determined by performing EDS analysis on cross-sectional samples and the results are presented in Table 6. The aluminum to titanium ratio was determined to be 3.76 and 1.97 for coatings deposited with 20 at.% Ti – 80 at.% Al and 33 at.% Ti – 67 at.% Al, respectively. Thus, the coating composition mimicked the cathode composition.

The as-deposited and corrosion tested 8-layer TiN/TiAlN coating results and discussions regarding their composition, phases and corrosion performance in static pure water at 360 °C and 18.7 MPa were provided in Alat et al. [50]. Yb-doped sample morphological and crystal structure analysis were also performed by using SEM and XRD. Additionally, Yb-doped sample compositions were measured using the energy dispersive spectroscopy (EDS) and confirmed by EPMA. Results and discussions regarding the as-deposited Yb-doped coatings are provided in Brova et al. [52].

4.3. Mechanical properties

In single-layer TiAlN coatings scratch tests, three main deformation mechanisms were observed through the scratch. Fig. 6 shows the SEM–SE, SEM-BSE and loading vs distance diagram of the corresponding scratch performed on a sample having a coating deposited with 25 V substrate bias. First observed deformation was the lateral cracks that started to form at 3 μm scratch length and 13.1 N load. Second deformation mode was the transverse cracks

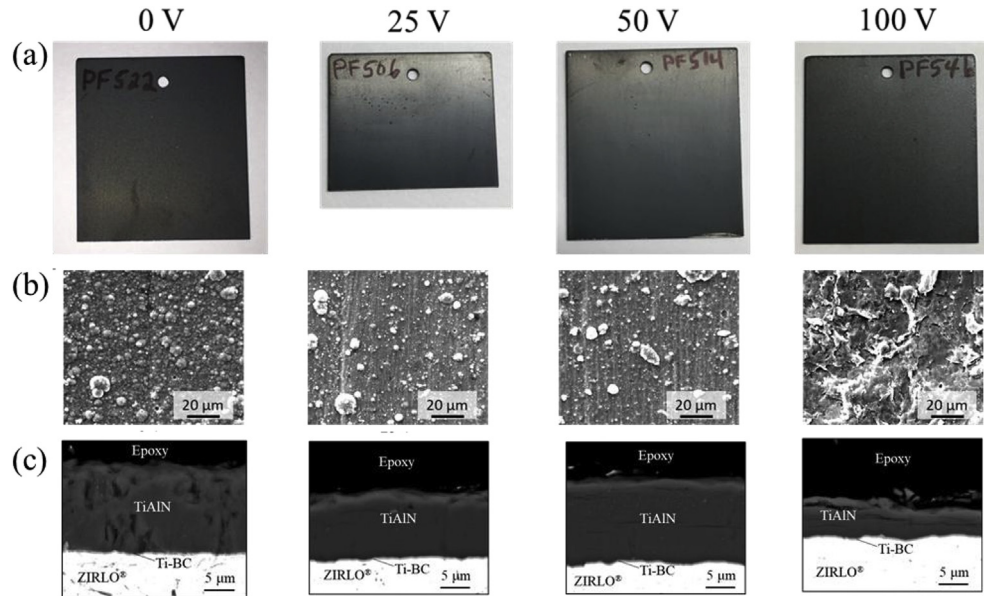


Fig. 3. (a) Digital images, (b) surface SEM–SE and (c) cross-section SEM–BSE images of TiAlN coated ZIRLO® sheets with four different substrate biases: 0 V, 25 V, 50 V and 100 V.

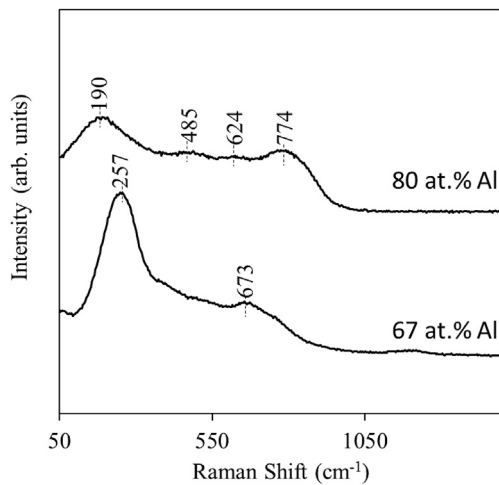


Fig. 4. Overlaid Raman spectrums of coatings deposited with cathodes having a composition of 33 at.% Ti – 67 at.% Al and 20 at.% Ti – 80 at.% Al.

assisted with chipping and buckling spallation that started to occur at 5.9 μm scratch length and 26.9 N load. Simultaneously, coating fragment detachments occurred at the rim of the scratch and recovery spallation was initiated at the two edges of the scratch because of combined adhesive and cohesive failure [76–78]. Finally, gross spallation of the coating occurred at 8.4 μm scratch length and 38.7 N load. The coating adhesion performance of coatings deposited with different substrate biases of 0 V, 25 V, 50 V and 100 V was evaluated by comparing the critical load to start gross spallation in each of the coatings. For the coating deposited with 100 V substrate bias, critical load to cause spallation was determined to be 2.9 N. In the coatings deposited with 0 V and 50 V, coating spallation was not observed even at the maximum loading of 48.5 and 47.9 N, respectively. No spallation in the case of coatings deposited with 0 V substrate bias can be attributed to a resilience achieved in the coating with a higher volume fraction of macroparticles. The higher critical load required for gross spallation in the case of 50 V substrate bias compared to 25 V can be attributed to

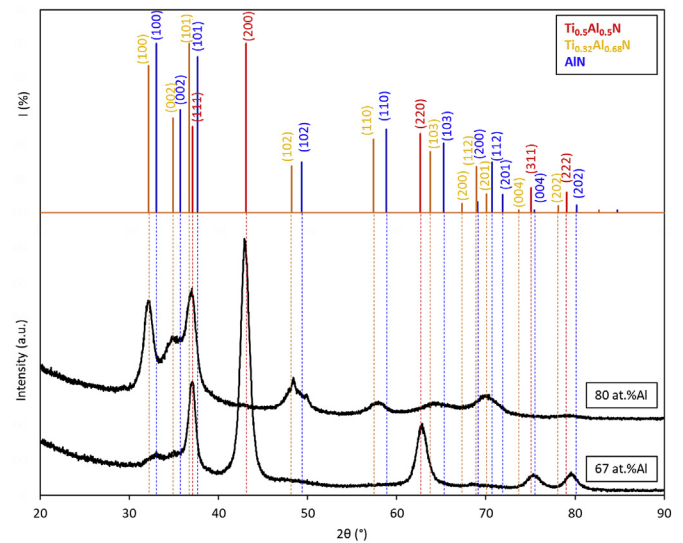


Fig. 5. GIXRD measurement patterns of coatings deposited with cathodes having a composition of 33 at.% Ti – 67 at.% Al and 20 at.% Ti – 80 at.% Al. XRD-GI was performed using a Cu-K α (1.54048 Å) radiation and with a grazing incidence angle of 1°.

the increased coating adhesion because of ejection of metal ions from the surface or ion penetration into the substrate lattice during ion bombardment leading to enhanced coating adhesion [36]. The low critical load in the case of 100 V substrate bias can be attributed to the rougher surface and high degree of residual stress [79].

Fig. 7 shows the SEM–BSE image of scratch tested single-layer TiAlN coatings deposited with two different cathode compositions of Ti_{0.20}Al_{0.80} and Ti_{0.33}Al_{0.67}. For the used scratch rate, gross spallation was not observed in coatings deposited with Ti_{0.33}Al_{0.67} cathode, indicating better adhesion compared to coatings deposited with Ti_{0.20}Al_{0.80} cathode. This can be attributed either to more aluminum concentration in TiAlN coating leading to higher microhardness difference between the substrate and the coating, and eventually critical load decrease [80] or to the lower surface roughness and better coating integrity due to less macroparticles

Table 6
Composition of TiAlN coatings deposited by using cathodes having 20 at.% Ti – 80 at.% Al and 33 at.% Ti – 67 at.% Al. Coating compositions were determined using energy dispersive spectroscopy (EDS) point analysis.

Cathode composition	Ti, at.%	Al, at.%	N, at.%	Ti, wt.%	Al, wt.%	N, wt.%
20 at.% Ti – 80 at.% Al	8.76 ± 0.20	32.98 ± 0.34	58.26 ± 0.50	19.73 ± 0.36	41.85 ± 0.29	38.39 ± 0.50
33 at.% Ti – 67 at.% Al	13.10 ± 0.47	25.83 ± 0.60	59.68 ± 2.34	28.71 ± 0.77	31.90 ± 0.54	38.26 ± 1.51

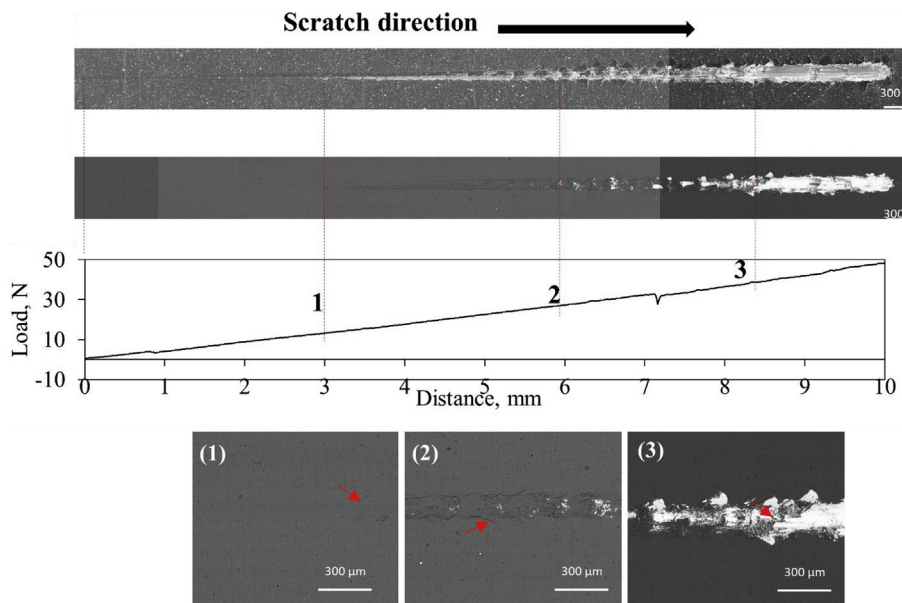


Fig. 6. SEM secondary electron (SE), SEM backscatter electron and loading vs distance diagram of the corresponding scratch performed on a sample having a TiAlN coating deposited with 25 V substrate bias, 60 A source current, cathode with 20 at.% Ti – 80 at.% Al.

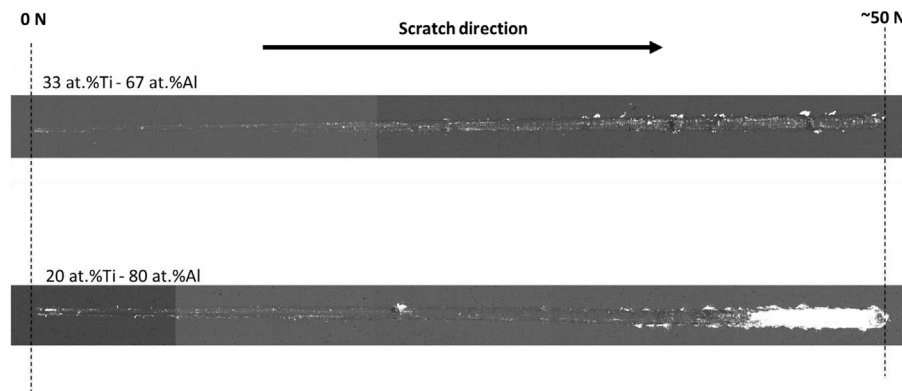


Fig. 7. SEM-BSE image of scratched TiAlN coatings deposited with 50 V substrate bias, 60 A source current, and using a cathode with 33 at.% Ti - 67 at.% Al or 20 at.% Ti - 80 at.% Al.

that can be attributed to less aluminum content [66,73,79].

Fig. 8 shows scratch testing result of 8-layer TiN/TiAlN coated ZIRLO® sheet having TiAlN layers deposited using 33 at.% Ti – 67 at.% Al with 75 V substrate bias and 45 A source current. Gross spallation observed to be occurring after 6.15 mm scratch distance at 27 N. The gross spallation location was also confirmed with energy dispersive spectroscopy (EDS) elemental map analysis shown in Fig. 8b that shows titanium, aluminum, nitrogen having regions and then zirconium appearance because of coating spallation. Fig. 9 shows scratch testing results of 8-layer TiN/TiAlN coated ZIRLO® sheet having TiAlN layers deposited using 20 at.% Ti – 80 at.% Al. The gross spallation onset took place at ~26 N. Based on these

results, it can be concluded that cathode composition variation did not affect coating adhesion significantly in the case of 8-layer TiN/TiAlN coating deposited with indicated deposition parameters. Additionally, as we compare critical load value to cause gross spallation in single-layer and multilayer coatings, we see that multilayer coatings require lower critical load which can be attributed to less Hertzian stress distribution due to thinner layers in the case of multilayer coatings.

Vickers microhardness testing was used to evaluate the effect of the ytterbium dopants on the mechanical integrity of the coatings. The hardness values (Fig. 10) were in the range of 2600–3500 HV [81]. As ytterbium content within the TiAlN coating increased,

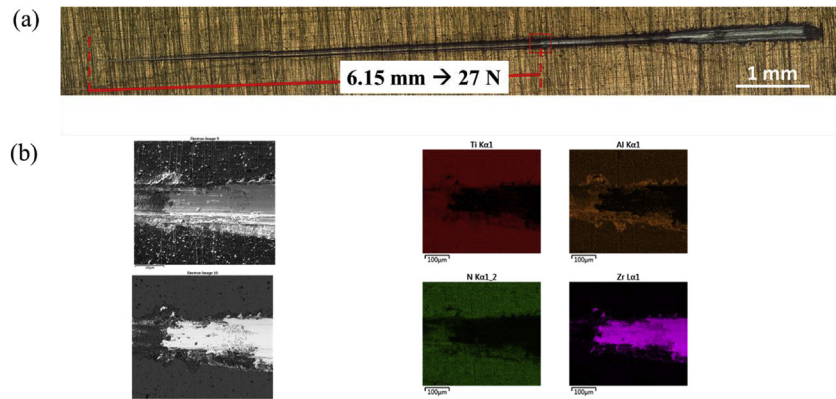


Fig. 8. (a) Optical microscopy image and (b) EDS-elemental map analysis of the scratch on green scotch brite prepared 8-layer TiN/TiAlN/Ti/ZIRLO[®] sheet. (TiAlN layer deposition parameters: cathode 33 at.% Ti – 67 at. % Al, 75 V substrate bias and 45 A source current. TiN layer deposition parameters: 150 V substrate bias and 45 A source current). (For interpretation of the references to color in this figure legend, the reader is referred to the Web version of this article.)

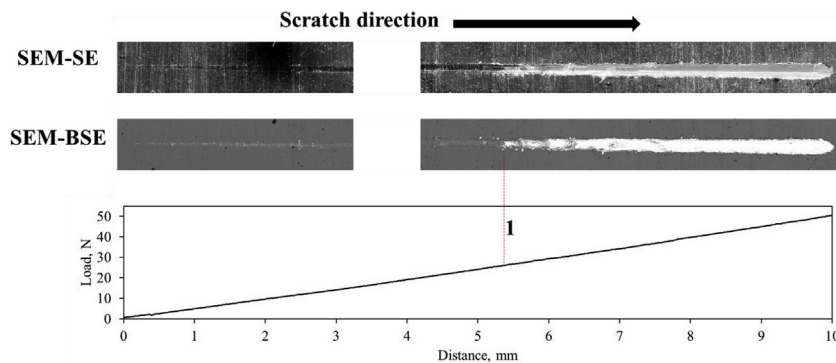


Fig. 9. Analysis of the scratch on green scotch brite prepared 8-layer TiN/TiAlN/Ti/ZIRLO[®] sheet. (TiAlN layer deposition parameters: cathode 20 at.% Ti – 80 at. % Al, 75 V substrate bias and 45 A source current. TiN layer deposition parameters: 150 V substrate bias and 45 A source current). (For interpretation of the references to color in this figure legend, the reader is referred to the Web version of this article.)

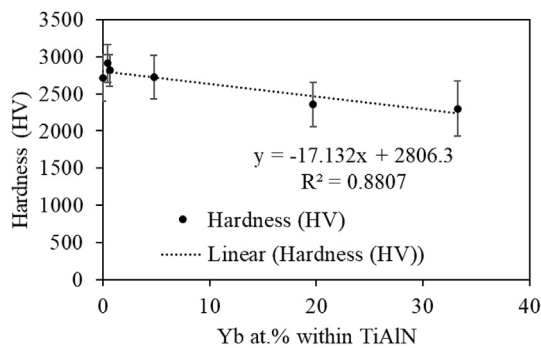


Fig. 10. Cross-section Vickers microhardness values with respect to Yb content in the TiAlN coatings deposited on ZIRLO[®] sheets.

hardness decreased. The higher concentrations of ytterbium resulted in an average loss of 464 HV. The decrease in hardness with increase in ytterbium content can be attributed to the increased metal content.

In all the coatings on ZIRLO[®] flats, scratch adhesion testing resulted in cohesive failure in the form of conformal cracking which can be seen in Fig. 11a. The scratch length of the critical load for conformal cracking was defined as the distance from the beginning of the scratch to the center of the first crack. The average normal force required to generate conformal cracking was 27.5 N. Adhesive

failure in the form of minor coating spallation also occurred with the conformal cracking and was consistent until the total adhesive failure of the coating. Fig. 11b shows the critical load values required to induce initial cohesive failure. While all coatings are relatively consistent in terms of critical loads, fluctuations in critical load is most likely due to processing differences such as riser usage during the deposition process. The cohesive failure is attributed to the method of doping not being optimized, combined with variation in the coating dopant gradation through the coating thickness.

Fig. 12a shows an optical micrograph of the characteristic total adhesive failure of the doped titanium aluminum nitride coating systems. Across all coatings, reaching the critical load would result in uniform and consistent coating removal. The average coating total adhesive failure occurred at 58.7 N. Fig. 12b shows the critical loads required to induce gross spallation within the ytterbium doped titanium aluminum nitride films. There is no trend between the amount of ytterbium within the film and the force required to achieve adhesive failure (coating delamination from substrate). This is most likely due to adhesive failure being dependent upon the thickness and quality of the bond coat in addition to coating preparation, thickness, stress, and microstructure. Minor processing differences in the bond coat may explain the slight variation within the data.

5. Conclusions

TiAlN, when combined in alternating layers with TiN, produces a

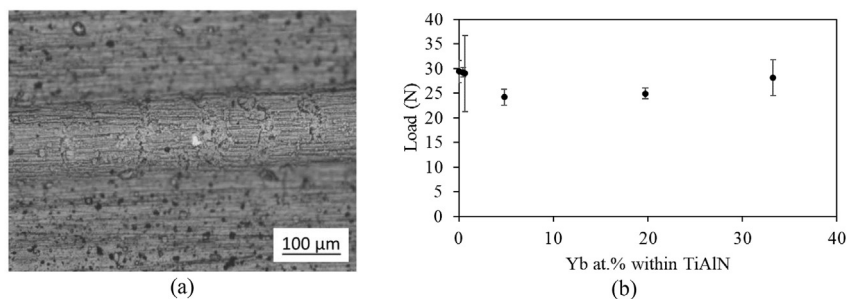


Fig. 11. (a) Optical microscopy image showing the conformal cracking consistent across all Yb-doped titanium aluminum nitride coatings as deposited on ZIRLO[®] sheets. (b) Adhesion critical load values required to induce confocal cracking and minor spallation with respect to Yb content in the TiAlN coatings deposited on ZIRLO[®] sheets.

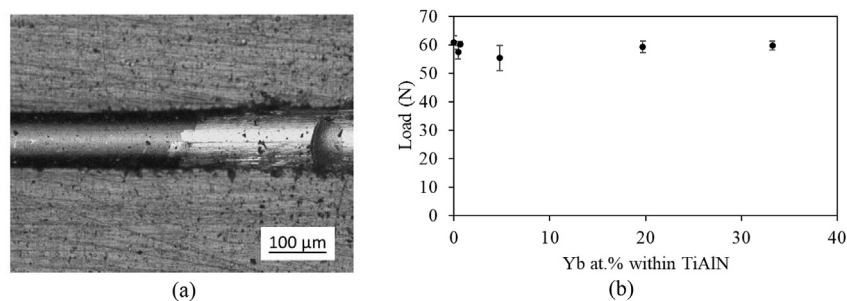


Fig. 12. (a) Optical microscopy image showing characteristic adhesive failure upon reaching a critical load, as the coatings uniformly exhibit gross spallation. (b) Critical loads required to induce gross spallation within Yb-doped titanium nitride films.

thin ceramic coating with improved corrosion resistance compared to bare zirconium-based alloys. However, to withstand higher temperatures, doping agents, yttrium and ytterbium, can modify TiAlN/TiN layers. The neutronic impact of adding monolithic TiN, monolithic TiAlN and 8-layer TiAlN/TiN coatings with and without dopants to the exterior of conventional UO₂/zirconium-alloy cladding was evaluated. Also, select coating design architectures were deposited by CA-PVD on ZIRLO[®] sheets and mechanically tested. The conclusions derived from neutronic analysis, and mechanical tests are as follows:

1. Minimizing the penalty derived from such coatings can be achieved by reducing coating thickness, decreasing the titanium concentration, increasing the yttrium concentration, and lowering the ytterbium concentration.
2. Nevertheless, in the worst-case scenario of a 12 μm 8-layer TiAlN/TiN coatings with high titanium and ytterbium concentrations, the overall neutronic impact is minor and the fuel enrichment compensation to maintain the reference cycle length does not exceed 0.1 at.%.
3. Substrate bias affects coating properties including coating color, density, macroparticle amount, surface roughness and residual stresses. There is an optimum substrate bias range to achieve dense, defect-free coatings. Too low substrate bias led to porous coatings with excessive amount of macroparticles. Too high substrate bias cause nonuniform and defective coatings.
4. Higher values of critical load to cause gross spallation was achieved in the case of single-layer TiAlN coatings compared to 8-layer TiN/TiAlN coating.
5. Microhardness indentation testing showed that the hardness of lightly doped coatings was similar to that of un-doped coating at 2793 HV.
6. Scratch adhesion testing revealed that all Yb-doped coatings initially experienced conformal cracking before undergoing

gross coating spallation. Coating adhesion was determined to be related to processing parameters rather than dopant concentrations.

Data availability statement

All data supporting the findings is fully available in the body of the manuscript. Additional datasets generated during the current study are available from the corresponding author on reasonable request.

Acknowledgements

This research was sponsored by the U.S. Department of Energy, Office of Nuclear Energy, Nuclear Energy University Program, under grant number DE-AC07-05ID14517. Westinghouse Electric Company LLC is acknowledged for providing ZIRLO[®] samples. The authors would like to thank Thomas P. Medill for his help in coating deposition, Jeremy M. Schreiber for his help in sample preparation, Maxwell Wetherington for his help in Raman spectroscopy and Thomas V. McKnight for his assistance during scratch tests.

Appendix A. Supplementary data

Supplementary data to this article can be found online at <https://doi.org/10.1016/j.jnucmat.2019.02.044>.

References

- [1] J. Conca, EROI– A Tool to Predict the Best Energy Mix, Forbes, 2015. <https://www.forbes.com/sites/jamesconca/2015/02/11/eroi-a-tool-to-predict-the-best-energy-mix/#7a7a47f6a027>.
- [2] M.F. Ashby, M. Smidman, Materials for Nuclear Power Systems, Granta Design, 2010. Version 1.1.
- [3] T. Alam, M.K. Khan, M. Pathak, K. Ravi, R. Singh, S.K. Gupta, A review on the

- clad failure studies, Nucl. Eng. Des. 241 (2011) 3658–3677, <https://doi.org/10.1016/j.nucengdes.2011.08.009>.
- [4] Z. Duan, H. Yang, Y. Satoh, K. Murakami, S. Kano, Z. Zhao, J. Shen, H. Abe, Current status of materials development of nuclear fuel cladding tubes for light water reactors, Nucl. Eng. Des. 316 (2017) 131–150, <https://doi.org/10.1016/j.nucengdes.2017.02.031>.
- [5] R. Krishnan, M.K. Asundi, Zirconium alloys in nuclear technology, Proc. Indian Acad. Sci. (Engg. Sei.) 4 (1981) 41–56.
- [6] T.R. Allen, R.J.M. Konings, A.T. Motta, Corrosion of zirconium alloys, in: Compr. Nucl. Mater., first ed., Elsevier Inc., 2012, pp. 49–68, <https://doi.org/10.1016/B978-0-08-056033-5.00063-X>.
- [7] S. Bragg-Sitton, Development of advanced accident-tolerant fuels for commercial LWRs, Nucl. News. (n.d.) 83–91.
- [8] K. Barrett, S. Bragg-Sitton, D. Galicki, Advanced LWR Nuclear Fuel Cladding System Development Trade-Off Study, Idaho National Laboratory, 2012. Report number: IN/Ext-12-27090.
- [9] R. Oelrich, P. Xu, E. Lahoda, C. Deck, Update on Westinghouse EnCore® accident tolerant fuel program, Trans. Am. Nucl. Soc. 118 (2018) 1311–1313.
- [10] J. Bischoff, C. Delafoy, N. Chaari, C. Vauglin, K. Buchanan, P. Barberis, E. Monsifrot, F. Schuster, J.-C. Brachet, K. Nimishakavi, CR-coated cladding development at framatome, in: Top Fuel 2018, 2018, p. A0152.
- [11] H. Yeom, B.R. Maier, G. Johnson, T. Dabney, M. Lenling, P. Scallion, J. Romero, J. Walters, P. Xu, H. Shah, K. Sridharan, Cold spray coatings for accident tolerant Zr-alloy cladding in light water reactors, in: Trans. Am. Nucl. Soc., 2018, pp. 1576–1579.
- [12] H. Kim, I. Kim, Y. Jung, D. Park, J. Park, J. Yang, Y. Koo, Progress of surface modified ZR cladding development for atf at kaeri, in: 2017 Water React. Fuel Perform. Meet., 2017, pp. 1–6.
- [13] J.C. Brachet, M. Dumerval, V. Lezaud-Chaillieux, M. Le Saux, E. Rousesne, D. Hamon, S. Urvoy, T. Guilbert, Q. Houmaire, C. Cobac, G. Nony, J. Rousselot, F. Lomello, F. Schuster, H. Palanchar, J. Bischoff, E. Pouillier, Behavior of chromium coated M5 TM claddings under LOCA, in: 2017 Water React. Fuel Perform. Meet., 2017, pp. 1–6.
- [14] L. Hallstadius, S. Johnson, E. Lahoda, Cladding for high performance fuel, Prog. Nucl. Energy 57 (2012) 71–76, <https://doi.org/10.1016/j.pnucene.2011.10.008>.
- [15] W.-J. Kim, D. Kim, J.Y. Park, Fabrication and material issues for the application of SiC composites to LWR fuel cladding, Nucl. Eng. Technol. 45 (2013) 565–572, <https://doi.org/10.5516/NET.07.2012.084>.
- [16] Y. Katoh, L.L. Snead, T. Nozawa, T. Hinoki, A. Kohyama, N. Igawa, T. Taguchi, Mechanical properties of chemically vapor-infiltrated silicon carbide structural composites with thin carbon interphases for fusion and advanced fission applications, Mater. Trans. 46 (2005) 527–535, <https://doi.org/10.2320/matertrans.46.527>.
- [17] Y. Katoh, L.L. Snead, C.H. Henager, T. Nozawa, T. Hinoki, A. Ivekovic, S. Novak, S.M. Gonzalez de Vicente, Current status and recent research achievements in SiC/SiC composites, J. Nucl. Mater. 455 (2014) 387–397, <https://doi.org/10.1016/j.jnucmat.2014.06.003>.
- [18] Y. Katoh, K. Ozawa, C. Shih, T. Nozawa, R.J. Shinavski, A. Hasegawa, L.L. Snead, Continuous SiC fiber, CVI SiC matrix composites for nuclear applications: properties and irradiation effects, J. Nucl. Mater. 448 (2014) 448–476, <https://doi.org/10.1016/j.jnucmat.2013.06.040>.
- [19] K. Yueh, K.A. Terrani, Silicon carbide composite for light water reactor fuel assembly applications, J. Nucl. Mater. 448 (2014) 380–388, <https://doi.org/10.1016/j.jnucmat.2013.12.004>.
- [20] C. Lorrette, C. Sauder, P. Billaud, C. Hossepied, G. Loupias, J. Braun, E. Torres, F. Rebillat, A. Michaux, J. Bischoff, A. Ambard, SiC/SiC composite behavior in LWR conditions and under high temperature steam environment, in: Top Fuel 2015, Zurich, Switzerland, 2015, pp. 126–134.
- [21] C.P. Deck, H.E. Khalifa, B. Sammulu, T. Hilsabeck, C.A. Back, Fabrication of SiC–SiC composites for fuel cladding in advanced reactor designs, Prog. Nucl. Energy 57 (2012) 38–45, <https://doi.org/10.1016/j.pnucene.2011.10.002>.
- [22] J.D. Stempien, D.M. Carpenter, G. Kohse, M.S. Kazimi, Characteristics of composite silicon carbide fuel cladding after irradiation under simulated PWR conditions nuclear systems, Nucl. Technol. 183 (2013) 13–29, <https://doi.org/10.13182/NT12-86>.
- [23] Y. Lee, M.S. Kazimi, A structural model for multi-layered ceramic cylinders and its application to silicon carbide cladding of light water reactor fuel, J. Nucl. Mater. 458 (2015) 87–105, <https://doi.org/10.1016/j.jnucmat.2014.12.013>.
- [24] C.H. Henager, E.A. Le, R.H. Jones, A model stress analysis of swelling in SiC/SiC composites as a function of fiber type and carbon interphase structure, J. Nucl. Mater. 329–333 (2004) 502–506, <https://doi.org/10.1016/j.jnucmat.2004.04.110>.
- [25] T. Nozawa, Y. Katoh, L.L. Snead, The effect of neutron irradiation on the fiber/matrix interphase of silicon carbide composites, J. Nucl. Mater. 384 (2009) 195–211, <https://doi.org/10.1016/j.jnucmat.2008.11.015>.
- [26] D. Kim, H.-G. Lee, J.Y. Park, W.-J. Kim, Fabrication and measurement of hoop strength of SiC triplex tube for nuclear fuel cladding applications, J. Nucl. Mater. 458 (2015) 29–36, <https://doi.org/10.1016/j.jnucmat.2014.11.117>.
- [27] J.C. Stone, R. Schleicher, C.P. Deck, G.M. Jacobsen, H.E. Khalifa, C.A. Back, Stress analysis and probabilistic assessment of multi-layer SiC-based accident tolerant nuclear fuel cladding, J. Nucl. Mater. 466 (2015) 682–697, <https://doi.org/10.1016/j.jnucmat.2015.08.001>.
- [28] M. Ben-Belgacem, V. Richet, K.A. Terrani, Y. Katoh, L.L. Snead, Thermo-mechanical analysis of LWR SiC/SiC composite cladding, J. Nucl. Mater. 447 (2014) 125–142, <https://doi.org/10.1016/j.jnucmat.2014.01.006>.
- [29] B. Cheng, Y.J. Kim, P. Chou, Improving accident tolerance of nuclear fuel with coated Mo-alloy cladding, Nucl. Eng. Technol. 48 (2016) 16–25, <https://doi.org/10.1016/j.net.2015.12.003>.
- [30] B.A. Pint, K.A. Terrani, Y. Yamamoto, L.L. Snead, Material selection for accident tolerant fuel cladding, Metall. Mater. Trans. E. 2 (2014) 190–196, <https://doi.org/10.1007/s40553-015-0056-7>.
- [31] R.B. Rebak, K.A. Terrani, W.P. Gassmann, J.B. Williams, K.L. Ledford, S. Nuclear, Improving nuclear power plant safety with FeCrAl alloy fuel cladding, MRS Adv 2 (2017) 1–8, <https://doi.org/10.1557/adv.2017>.
- [32] K.A. Terrani, S.J. Zinkle, L.L. Snead, Advanced oxidation-resistant iron-based alloys for LWR fuel cladding, J. Nucl. Mater. 448 (2014) 420–435, <https://doi.org/10.1016/j.jnucmat.2013.06.041>.
- [33] M. Kurata, Research and development methodology for practical use of accident tolerant fuel in light water reactors, Nucl. Eng. Technol. 48 (2016) 26–32, <https://doi.org/10.1016/j.net.2015.12.004>.
- [34] C. Tang, M. Stueber, H.J. Seifert, M. Steinbrueck, Protective coatings on zirconium-based alloys as accident-tolerant fuel (ATF) claddings, Corros. Rev. 35 (2017) 141–165, <https://doi.org/10.1515/corrrev-2017-0010>.
- [35] R.J. Comstock, Zirconium in the Nuclear Industry (1979), <https://doi.org/10.1520/STP681-EB>.
- [36] S. PalDey, S. Deevi, Single layer and multilayer wear resistant coatings of (Ti, Al) N: a review, Mater. Sci. Eng. 342 (2003) 58–79, [https://doi.org/10.1016/S0921-5093\(03\)00473-8](https://doi.org/10.1016/S0921-5093(03)00473-8).
- [37] S.K. Han, G. Jeon, Joo S. Yoon, Hyung J. Kim, High temperature wear resistance of (TiAl)N films synthesized by cathodic arc plasma deposition, Surf. Coating. Technol. 86–87 (1996) 82–87.
- [38] K.L. Lin, M.Y. Hwang, C.D. Wu, The deposition and wear properties of cathodic arc plasma deposition TiAlN deposits, Mater. Chem. Phys. 46 (1996) 77–83, [https://doi.org/10.1016/0254-0584\(96\)80134-9](https://doi.org/10.1016/0254-0584(96)80134-9).
- [39] J.G. Han, K.H. Nam, I.S. Choi, The shear impact wear behavior of Ti compound coatings, Wear 214 (1998) 91–97, [https://doi.org/10.1016/S0043-1648\(97\)00205-6](https://doi.org/10.1016/S0043-1648(97)00205-6).
- [40] Y. Wang, A study of PVD coatings and die materials for extended die-casting die life, Surf. Coating. Technol. 94–95 (1997) 60–63, [https://doi.org/10.1016/S0257-8972\(97\)00476-3](https://doi.org/10.1016/S0257-8972(97)00476-3).
- [41] T. Suzuki, D. Huang, Y. Ikuhara, Microstructures and grain boundaries of (Ti,Al) N films, Surf. Coating. Technol. 107 (1998) 41–47, [https://doi.org/10.1016/S0257-8972\(98\)00550-7](https://doi.org/10.1016/S0257-8972(98)00550-7).
- [42] R.D. James, D.L. Paisley, K.A. Gruss, S. Parthasarathi, B.R. Tittmann, Y. Horie, R.F. Davis, Adhesion evaluation of TiN and (Ti, Al)N coatings on titanium 6Al-4V, Mater. Res. Soc. Symp. Proc. 410 (1996) 377–382.
- [43] A. Anders, A review comparing cathodic arcs and high power impulse magnetron sputtering (HiPIMS), Surf. Coating. Technol. 257 (2014) 308–325, <https://doi.org/10.1016/j.surfcoat.2014.08.043>.
- [44] E. Lugscheider, C. Barimani, C. Wolff, S. Guerreiro, G. Doepper, Comparison of the structure of PVD-thin films deposited with different deposition energies, Surf. Coating. Technol. 86–87 (1996) 177–183.
- [45] R.L. Boxman, D.M. Sanders, P.J. Martin (Eds.), Handbook of Vacuum Arc Science and Technology: Fundamentals and Applications, Noyes Publications, Park Ridge, New Jersey, 1995.
- [46] A. Anders, Cathodic arc plasma deposition, Vac. Technol. Coat. 3 (2002) 1–26, [https://doi.org/10.1016/0040-6090\(88\)90494-4](https://doi.org/10.1016/0040-6090(88)90494-4).
- [47] W.D. Sproul, Physical vapor deposition tool coatings, Surf. Coating. Technol. 81 (1996) 1–7, [https://doi.org/10.1016/0257-8972\(95\)02616-9](https://doi.org/10.1016/0257-8972(95)02616-9).
- [48] M. Ahlgren, H. Blomqvist, Influence of bias variation on residual stress and texture in TiAlN PVD coatings, Surf. Coating. Technol. 200 (2005) 157–160, <https://doi.org/10.1016/j.surfcoat.2005.02.078>.
- [49] E. Alat, A.T. Motta, R.J. Comstock, J.M. Partezana, D.E. Wolfe, Ceramic coating for corrosion (c3) resistance of nuclear fuel cladding, Surf. Coating. Technol. 281 (2015) 133–143, <https://doi.org/10.1016/j.surfcoat.2015.08.062>.
- [50] E. Alat, A.T. Motta, R.J. Comstock, J.M. Partezana, D.E. Wolfe, Multilayer (TiN, TiAlN) ceramic coatings for nuclear fuel cladding, J. Nucl. Mater. 478 (2016) 236–244, <https://doi.org/10.1016/j.jnucmat.2016.05.021>.
- [51] I.J. Smith, W.D. Münz, L.A. Donohue, I. Petrov, J.E. Greene, Improved Ti1–xAlxN PVD coatings for dry high speed cutting operations, Surf. Eng. 14 (1998) 37–42, <https://doi.org/10.1179/sur.1998.14.1.37>.
- [52] M.J. Brova, E. Alat, M.A. Pauley, R. Sherbondy, A.T. Motta, D.E. Wolfe, Undoped and ytterbium-doped titanium aluminum nitride coatings for improved oxidation behavior of nuclear fuel cladding, Surf. Coating. Technol. 331 (2017), <https://doi.org/10.1016/j.surfcoat.2017.09.076>.
- [53] N.R. Brown, H. Ludwig, A. Aronson, G. Raitzes, M. Todosow, Neutronic evaluation of a PWR with fully ceramic microencapsulated fuel. Part I: lattice benchmarking, cycle length, and reactivity coefficients, Ann. Nucl. Energy 62 (2013) 538–547, <https://doi.org/10.1016/j.anucene.2013.05.025>.
- [54] S. Chen, C. Yuan, Neutronic analysis on potential accident tolerant fuel-cladding combination U3Si2–FeCrAl, Sci. Technol. Nucl. Install (2017), <https://doi.org/10.1155/2017/3146985> (2017).
- [55] X. Wu, T. Kozłowski, J.D. Hales, Neutronics and fuel performance evaluation of accident tolerant FeCrAl cladding under normal operation conditions, Ann. Nucl. Energy 85 (2015) 763–775, <https://doi.org/10.1016/j.anucene.2015.06.032>.
- [56] O. Novák, M. Ševěček, Neutronic analysis of the candidate multi-layer cladding materials with enhanced accident tolerance for VVER reactor, in: 2017 Water React. Fuel Perform. Meet., 2017.

- [57] N.M. George, K. Terrani, J. Powers, A. Worrall, I. Maldonado, Neutronic analysis of candidate accident-tolerant cladding concepts in pressurized water reactors, *Ann. Nucl. Energy* 75 (2015) 703–712, <https://doi.org/10.1016/j.anucene.2014.09.005>.
- [58] I. Younker, M. Fratoni, Neutronic evaluation of coating and cladding materials for accident tolerant fuels, *Prog. Nucl. Energy* 88 (2016) 10–18, <https://doi.org/10.1016/j.pnucene.2015.11.006>.
- [59] J. Leppanen, PSG2/Serpent- S Continuous-Energy Monte Carlo Reactor Physics Burnup Calculation Code, 2012.
- [60] Westinghouse Electric Company LLC, CHAPTER 4 AP1000 Design Control Document 4, Reactor AP1000 Design Control Document, 2011, pp. 1–12.
- [61] M. Fratoni, E. Greenspan, Neutronic design of hydride fueled BWRs, *Nucl. Eng. Des.* 239 (2009) 1531–1543, <https://doi.org/10.1016/j.nucengdes.2009.01.016>.
- [62] ASTM C1624-05 Standard Test Method for Adhesion Strength and Mechanical Failure Modes of Ceramic Coatings by Quantitative Single Point Scratch Testing vol. 05 (2009) 1–29, <https://doi.org/10.1520/C1624-05R15> (Scope).
- [63] H.C. Barshilia, M.S. Prakash, A. Jain, K.S. Rajam, Structure, hardness and thermal stability of TiAlN and nanolayered TiAlN/CrN multilayer films, *Vacuum* 77 (2005) 169–179, <https://doi.org/10.1016/j.vacuum.2004.08.020>.
- [64] K. Sato, N. Ichimiya, A. Kondo, Y. Tanaka, Microstructure and mechanical properties of cathodic arc ion-plated (Al,Ti)N coatings, *Surf. Coating. Technol.* 163–164 (2003) 135–143, [https://doi.org/10.1016/S0257-8972\(02\)00610-2](https://doi.org/10.1016/S0257-8972(02)00610-2).
- [65] B.A. Eizner, G.V. Markov, A.A. Minevich, Deposition stages and applications of CAE multicomponent coatings, *Surf. Coating. Technol.* 79 (1996) 178–191, [https://doi.org/10.1016/0257-8972\(95\)02427-1](https://doi.org/10.1016/0257-8972(95)02427-1).
- [66] B.F. Coll, R. Fontana, A. Gates, P. Sathrum, (Ti-Al)N advanced films prepared by arc process, *Mater. Sci. Eng.* 140 (1991) 816–824, [https://doi.org/10.1016/0921-5093\(91\)90519-S](https://doi.org/10.1016/0921-5093(91)90519-S).
- [67] L. Karlsson, L. Hultman, M.P. Johansson, J.-E. Sundgren, H. Ljungcrantz, Growth, microstructure, and mechanical properties of arc evaporated Ti_xN_{1-x} (0 ≤ x ≤ 1) films, *Surf. Coating. Technol.* 126 (2000) 1–14, [https://doi.org/10.1016/S0257-8972\(00\)00518-1](https://doi.org/10.1016/S0257-8972(00)00518-1).
- [68] C. Gautier, J. Machet, Study of the growth mechanisms of chromium nitride films deposited by vacuum ARC evaporation, *Thin Solid Films* 295 (1997) 43–52, [https://doi.org/10.1016/S0040-6090\(96\)09164-X](https://doi.org/10.1016/S0040-6090(96)09164-X).
- [69] W.D. Münz, D.B. Lewis, S. Creasey, T. Hurkmans, T. Trinh, W. Ijzendorp, Defects in TiN and TiAlN coatings grown by combined cathodic arc/unbalanced magnetron technology, *Vacuum* 46 (1995) 323–330, [https://doi.org/10.1016/0042-207X\(94\)E0029-X](https://doi.org/10.1016/0042-207X(94)E0029-X).
- [70] H. Freller, H. Haessler, Ti_xAl_{1-x}N films deposited by ion plating with an arc evaporator, *Thin Solid Films* 153 (1987) 67–74, [https://doi.org/10.1016/0040-6090\(87\)90170-2](https://doi.org/10.1016/0040-6090(87)90170-2).
- [71] E. Erturk, H.-J. Heuvel, Adhesion and structure of TiN arc coatings, *Thin Solid Films* 153 (1987) 135–147.
- [72] A.N. Kale, K. Ravindranath, D.C. Kothari, P.M. Raole, Tribological properties of (Ti,Al)N coatings deposited at different bias voltages using the cathodic arc technique, *Surf. Coating. Technol.* 145 (2001) 60–70, [https://doi.org/10.1016/S0257-8972\(01\)01296-8](https://doi.org/10.1016/S0257-8972(01)01296-8).
- [73] S. PalDey, S.C. Deevi, Properties of single layer and gradient (Ti,Al)N coatings, *Mater. Sci. Eng.* 361 (2003) 1–8, [https://doi.org/10.1016/S0921-5093\(03\)00473-8](https://doi.org/10.1016/S0921-5093(03)00473-8).
- [74] C.P. Constable, J. Yarwood, W.-D. Münz, Raman microscopic studies of PVD hard coatings, *Surf. Coating. Technol.* 116–119 (1999) 155–159, [https://doi.org/10.1016/S0257-8972\(99\)00072-9](https://doi.org/10.1016/S0257-8972(99)00072-9).
- [75] H.C. Barshilia, K.S. Rajam, Raman spectroscopy studies on the thermal stability of TiN, CrN, TiAlN coatings and nanolayered TiN/CrN, TiAlN/CrN multilayer coatings, *J. Mater. Res.* 19 (2004) 3196–3205, <https://doi.org/10.1557/JMR.2004.0444>.
- [76] S. Sveen, J.M. Andersson, R. M'Saoubi, M. Olsson, Scratch adhesion characteristics of PVD TiAlN deposited on high speed steel, cemented carbide and PCBN substrates, *Wear* 308 (2013) 133–141, <https://doi.org/10.1016/j.wear.2013.08.025>.
- [77] S.J. Bull, Failure modes in scratch adhesion testing, *Surf. Coating. Technol.* 50 (1991) 25–32, [https://doi.org/10.1016/0257-8972\(91\)90188-3](https://doi.org/10.1016/0257-8972(91)90188-3).
- [78] P.J. Burnett, D.S. Rickerby, The relationship between hardness and scratch adhesion, *Thin Solid Films* 154 (1987) 403–416, [https://doi.org/10.1016/0040-6090\(87\)90382-8](https://doi.org/10.1016/0040-6090(87)90382-8).
- [79] P.J. Blau, Chapter 7, scratch adhesion testing, in: *Lab Handb. Scratch Testing*, Blue Rock Technical Publ., Oak Ridge, TN, 2002, pp. 7.1–7.15.
- [80] D. Wang, C. Chang, K. Wong, Y. Li, W. Ho, Improvement of the interfacial integrity of (Ti, Al)N hard coatings deposited on high speed steel cutting tools, *Surf. Coating. Technol.* 121 (1999) 388–394.
- [81] V.P. Astakhov, *Drills: Science Technology of Advanced Operations*, CRC Press, 2014.